

Superconducting THz sources with 12% power efficiency

R. Cattaneo¹, E. A. Borodiansky¹, A. A. Kalenyuk^{2,1}, and V. M. Krasnov^{1,3*}

¹ *Department of Physics, Stockholm University, AlbaNova University Center, SE-10691 Stockholm, Sweden;*

² *Institute of Metal Physics of National Academy of Sciences of Ukraine, 03142 Kyiv, Ukraine; and*

³ *Moscow Institute of Physics and Technology, State University, 9 Institutskiy per., 141700 Dolgoprudny, Russia;*

Low power efficiency is one of the main problems of THz sources, colloquially known as “the THz gap”. In this work we present prototypes of THz devices based on whisker-crystals of a high-temperature superconductor $\text{Bi}_2\text{Sr}_2\text{CaCu}_2\text{O}_{8+\delta}$ with a record high radiation power efficiency of 12% at a frequency of ~ 4 THz. We employ various on- and off-chip detection techniques and, in particular, use the radiative cooling phenomenon for accurate evaluation of the emission power. We argue that such devices can be used for creation of tunable, monochromatic, continuous-wave, compact and power-efficient THz sources.

Tunable, monochromatic, continuous-wave (CW), compact and power-efficient sources of terahertz (THz) electromagnetic waves (EMW) are required for a broad variety of applications such as spectroscopy, environmental control, security, non-ionizing medical imaging, ultra-high-speed telecommunication and electronics, as well as for fundamental research in various areas of science [1, 2]. The key problem of THz sources, colloquially known as the “THz gap”, is a rapid decay of radiation power efficiency (RPE), i.e. the ratio of emitted and dissipated power [3], in the low THz range [1]. Despite a significant progress, achieved in development of semiconducting quantum cascade lasers (QCL’s) [4–6], the RPE of CW QCL’s drops from $\simeq 28\%$ at $f \simeq 55$ THz [7] to a sub-percent at 3–4 THz [8, 9] and to $\sim 0.01\%$ at $f \simeq 1.3$ THz [10]. Although QCL frequency can be tuned [4, 5, 9, 11, 12], this comes at the expense of a dramatic reduction of RPE to $\sim 0.0001\%$ [11] when low THz emission is obtained by mixing or downconversion of higher frequencies [11, 12]. QCL’s emitting at primary low THz frequencies, on the other hand, have to be cooled down to cryogenic temperatures, $k_B T \lesssim hf$ [8–10].

Superconducting devices, based on arrays of Josephson junctions (JJ’s) have an inherent frequency tunability and provide an alternative technology for creation of cryogenic THz sources with tunable, monochromatic CW operation [13–30]. The Josephson frequency, $f_J = (2e/h)V$, is proportional to the dc-bias voltage V and is limited only by the superconducting energy gap, which can be in excess of 30 THz for high- T_c superconductors [31, 32]. Emission with a sub-mW power at $f \simeq 0.5$ THz was achieved from large-area mesa structures etched on top of single crystals of a layered cuprate superconductor $\text{Bi}_2\text{Sr}_2\text{CaCu}_2\text{O}_{8+\delta}$ (Bi-2212) [17]. Such mesas represent stacks of atomic scale intrinsic JJ’s [33]. Tunable EMW emission at the primary Josephson frequency in the whole THz range 1–11 THz has been reported from small-area Bi-2212 mesas [21], albeit with a lower power. The RPE for both large [17] and small [21] mesas on Bi-2212 single crystals is $\lesssim 1\%$, which is decent

for THz sources, but small compared to the theoretical limit of 50% [34]. The suboptimal operation is caused by impedance mismatching between a device and an open space. Another key limitation for all cryogenic devices is set by self-heating. Taking into account limited cooling power of compact cryo-refrigerators (sub-Watt at low T), devices with RPE $\sim 1\%$ would not be able to emit much more than 1 mW. Therefore, further enhancement of the emission power from compact cryogenic devices may only be achieved via enhancement of RPE.

Here we present prototypes of novel THz sources based on Bi-2212 whisker-type crystals with intermediate-size mesa structures. We employ various techniques for detection of THz radiation such as an *in-situ* detection by a mesa on the same whisker, an on-chip detection by electrically isolated mesa and an off-chip detection by a bolometer. Furthermore, we employ the radiative cooling phenomenon for estimation of the absolute value of the emitted power. It reveals that the RPE of our devices can reach 12% making a significant step forward towards the theoretical limit of 50%. The boost of efficiency is attributed to a good impedances matching with open-space, caused by a specific turnstile antenna-like geometry of our devices. We argue that such devices can be used for creation of tunable, and, most importantly power-efficient THz sources.

Figures 1 (a) and (b) show an image and a sketch of studied devices. In the middle of each device there is a Bi-2212 whisker crystal with typical sizes $(300 - 500) \times (20 - 30) \times (1 - 5) \mu\text{m}^3$ along crystallographic a , b and c -axes, respectively. Several metallic electrodes with the width $10 - 15 \mu\text{m}$ are made across the whisker. Beneath each electrode there is a mesa structure containing $N \sim 150 - 250$ intrinsic JJ’s. Devices are made by conventional microfabrication techniques. Details about sample fabrication and the experimental setup can be found in Ref. [21, 32] and the Supplementary [35].

Fig. 1 (c) shows the current-voltage (I - V) characteristics of a mesa at $T \simeq 3$ K. It consists of multiple branches, due to one-by-one switching of JJ’s from the superconducting to the resistive state [31–33]. The total number of JJ’s, $N \simeq 150 \pm 10$ for this mesa, is obtained by counting branches. A rough estimation, valid for all our

* Vladimir.Krasnov@fysik.su.se

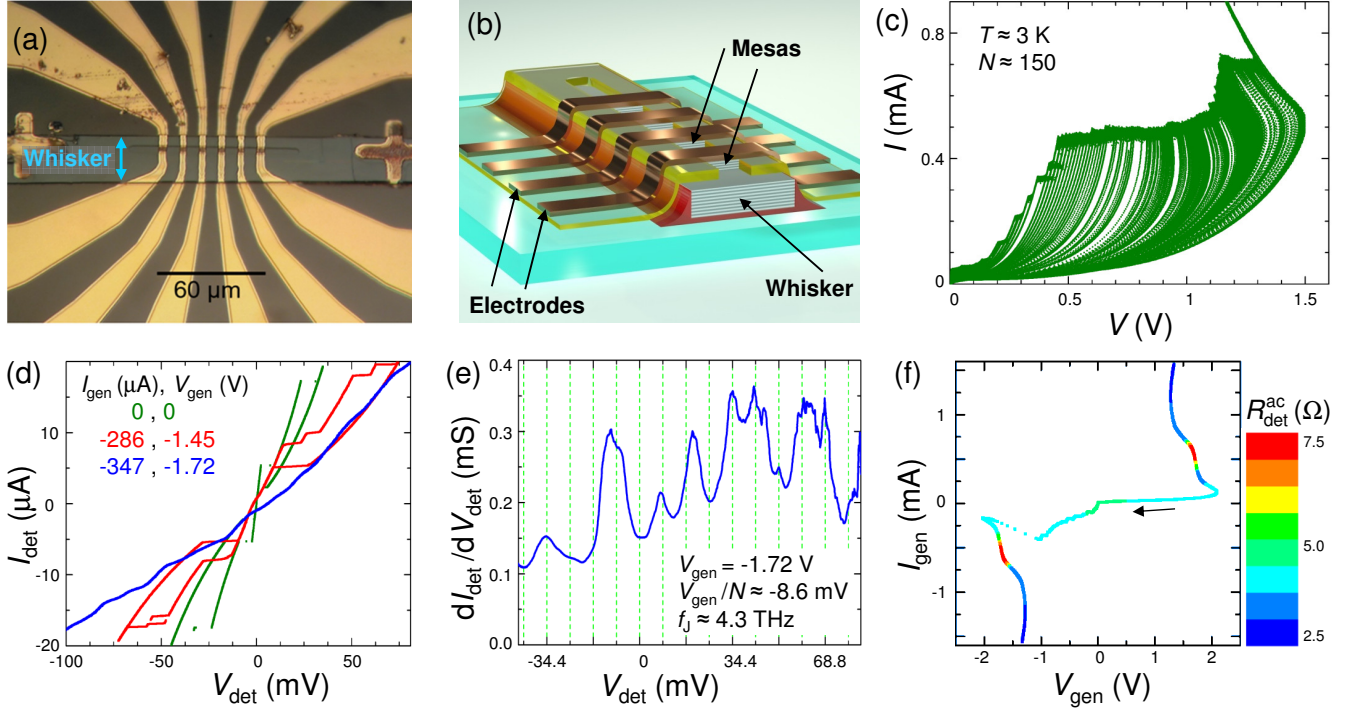


FIG. 1. (Color online). (a) Optical image of one of the studied devices. Six mesas are formed beneath gold electrodes. (b) A sketch of the device. (c) The I - V characteristics (integrated oscillogram) of a mesa. Multiple branches correspond to switching of individual, $N \simeq 150$, JJ's from superconducting to resistive state. (d) I - V curves of a detector mesa at three bias points in the generator, marked by circles in Fig. 2 (a). (e) Differential conductance of the blue I - V from (d). Peaks represent current steps. Grid lines corresponds to expected Shapiro step voltages. (f) On-chip generation-detection experiment with electrically disconnected mesas: Here we plot I - V of the generator mesa, color mapped by the ac-resistance of electrically separated detector mesa on the same chip. The black arrow indicates the bias sweep direction. It is seen that the emission (red color) occurs at steps in the I - V .

mesas is $N \simeq V_{max}/10$ mV, where V_{max} is the voltage at a maximum in the I - V . The maximum is caused by back-bending at high bias due to self-heating. The extent of self-heating depends on geometry and decreases with decreasing mesa sizes [36, 37]. Sizes of our mesas are in the range $(2.5 - 10) \times (10 - 30) \mu\text{m}^2$ with areas $50 < A < 300 \mu\text{m}^2$, which are significantly smaller than “large” mesas ($A > 10^4 \mu\text{m}^2$) studied in the majority of earlier works [16–20, 23–29], but larger than “small” mesas ($A \lesssim 10 \mu\text{m}^2$) studied in Ref. [21]. Thus, our mesas are of “intermediate size”. This enables a significant overall power ~ 1 mW with a tolerable self-heating.

To analyze EMW emission, we start with an on-chip generation-detection scheme [21] using one mesa as a generator and another mesa on the same chip as a switching-current detector. Figure 1 (d) shows evolution of the I - V 's of the detector at three bias points (I_{gen}, V_{gen}) in the generator. The I - V of the generator mesa, with marked bias points, is shown in the top panel of Fig. 2 (a). From Fig. 1 (d) it is seen that with increasing bias in the generator, critical currents in the detector are first reduced (red curve) and then get completely suppressed (blue curve) due to the EMW absorption [21]. Detailed dynamics of the generation-detection experiment is demon-

strated in the supplementary video [35].

Absorption of EMW by a JJ leads to formation of Shapiro steps in the I - V at $V_n = nhf/2e$ (n -integer). Thus, junction response carries a spectroscopic information both about the frequency and the amplitude of EMW. In mesas with N JJ's, the EMW emission occurs at $f_J = 2eV_{gen}/Nh$ (provided all JJ's are synchronized). Thus, the primary Shapiro step should appear at $V_{det} = V_{gen}/N$. Small steps can indeed be seen in the blue I - V from Fig. 1 (d). Fig. 1 (e) shows the differential conductance for this curve. It exhibits clear peaks, corresponding to steps in the I - V . The grid spacing is equal to V_{gen}/N with estimated $N \simeq 200$ for the generator mesa, see Fig. 2(a), and is in agreement with the observed peak separation. Some displacement of peak positions is likely caused by the fact that the detector response involves six JJ's, see Fig. 1 (d). A certain difference between JJ's leads to a mismatch of bias conditions for appearance of Shapiro steps. This affects both the regularity and the amplitude of Shapiro steps. Nevertheless, the data is consistent with occurrence of monochromatic emission at $f_J \simeq 4.3$ THz because the non-monochromatic emission would not lead to appearance of distinct steps.

To exclude possible electrical crosstalk, we performed

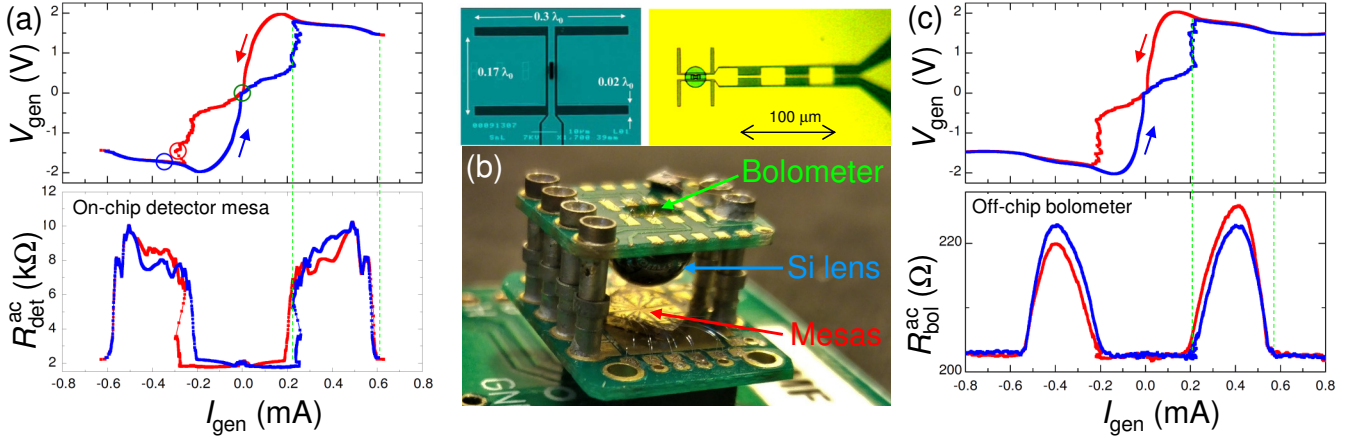


FIG. 2. (Color online). Comparison of on-chip and off-chip detection schemes. (a) On-chip generation-detection with electrically connected mesas. Top panel: the V - I of a generator mesa at $T \simeq 3$ K. Circles represent bias points for the detector I - V 's in Fig. 1 (d). Bottom: ac-resistance of the detector mesa as a function of the generator current. Blue/red curves represent up and down bias sweeps. (b) A setup for off-chip detection of emission by a NbN bolometer and images of the bolometer (from Refs. [38, 39]). (c) Off-chip detection experiment. Top: The V - I of the generator mesa. Bottom: the bolometer response as a function of I_{gen} . Vertical dashed lines in (a) and (c) indicate that emission occurs at the step in the generator I - V .

similar generation-detection experiment using electrically disconnected mesas. For this the whisker was cut by a focused ion beam in two sections, thus separating the generator and the detector mesas. The detector response remains qualitatively unchanged after such separation. Fig. 1 (f) shows the I - V of the generator mesa, color mapped by the response of electrically disconnected detector mesa (ac-resistance, R_{det}^{ac} , measured by the lock-in technique with zero offset). It is seen that a profound, almost vertical step develops in the back-bending region of the I - V . The color code indicates that the detector response appears just at this step and disappears both above and below. In Fig. 2 (a) the same behavior is demonstrated for the on-chip generation-detection experiment with electrically connected mesas. Here a correlation between the step in the I - V of the generator and the upturn in the detector response is clearly seen (see also the Supplementary video [35]). Such a non-monotonous behavior precludes self-heating origin of the observed signal and confirms occurrence of the EMW emission [21].

To confirm EMW emission into open space we perform off-chip detection using a NbN bolometer [38]. Fig. 2 (b) shows the measurement setup and images of the bolometer (from Refs. [38, 39]). The bolometer is placed at a distance ~ 1 cm above the device. Fig. 2 (c) shows corresponding generation (top) and detection (bottom) characteristics. Vertical dashed lines indicate that the bolometer response (lock-in resistance R_{bol}^{ac}) appears at the step in I_{gen} - V_{gen} , thus confirming EMW emission. Some difference in the shapes of on-chip, Fig. 2 (a), and off-chip, Fig. 2 (c), responses is likely caused by the spectral selectivity of the double-slot antenna of the bolometer, peaked at $f \simeq 1.6$ THz, well below the emission frequency $f_J \simeq 4.2$ THz for this mesa [40].

Power dissipation leads to heating, but EMW emis-

sion – to radiative cooling of the device. We use this for unambiguous estimation of the emission power, P_{THz} . Figure 3 (a) represents the on-chip generation-detection measurement for another device (upward bias sweep). The sample stage of our dry cryostat has a relatively small heat capacitance and a finite heat resistance, R_{th} , to the coldhead. Therefore, its temperature directly reflects the energy balance at the chip. Fig. 3 (b) shows the stage temperature as a function of the dissipation power, $P_{gen} = I_{gen}V_{gen}$, for the data from Fig. 3 (a). As expected from the Newton's law of cooling, it increases approximately linearly, $T_{stage} \simeq T_0 + R_{th}P_{gen}$, with $R_{th} = 0.508$ K/mW. However, at $P_{gen} \simeq 0.6$ mW there is a visible drop down from the linear dependence. In Fig. 3 (c) we plot this drop, ΔT , vs. I_{gen} . It clearly follows the detector response, shown by the red line in Fig. 3 (a). The correlation between ΔT and the EMW emission provides a straightforward demonstration of the radiative cooling phenomenon. Importantly, it allows direct estimation of $P_{THz} = \Delta T/R_{th}$. The maximum drop $\Delta T = -31.5 \pm 2$ mK occurs at $I_{gen} \simeq 0.4$ mA and $P_{gen} = 0.6$ mW. This yields $P_{THz} \simeq 62$ μ W and RPE of $10.3 \pm 0.7\%$ for this device.

Figs. 3 (d-f) show similar measurements for another device. Fig. 3 (d) shows V_{gen} (blue, left axis) and R_{det}^{ac} (red, right axis) vs. P_{gen} for the upward bias sweep (black lines represent similar data for the reverse sweep). The dark blue curve in Fig. 3 (e) shows T_{stage} vs. P_{gen} for the upward sweep. Inset shows time dependence of $P_{gen}(t)$ during this sweep. It is nonlinear due to the non-Ohmic I - V of the generator. The nonlinearity may cause some transient effects. Therefore, to make an accurate calibration of the bare (without device) thermal response of the stage we heated it by a resistor, applying exactly the same time-dependence of the dissipation power using a

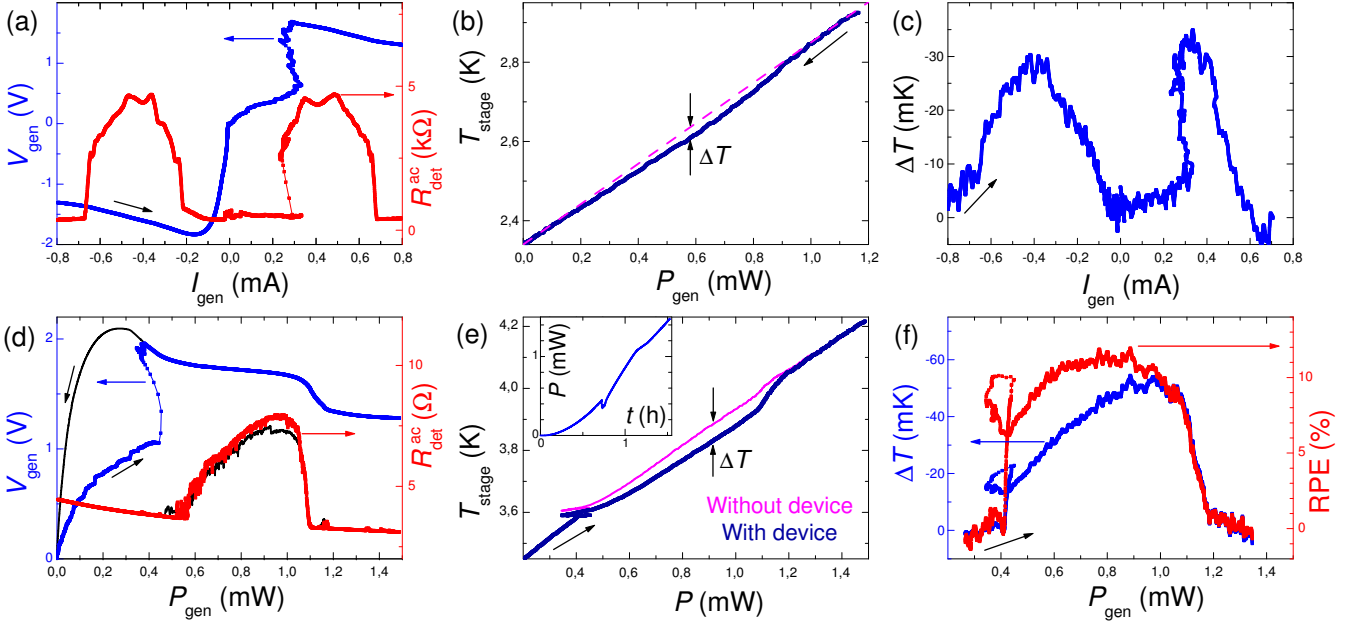


FIG. 3. (Color online). Radiative cooling analysis of emission for two devices (a-c) and (d-f). (a) The generator V - I (blue, left axis) and the on-chip detector response (red, right axis) vs. I_{gen} . (b) The stage temperature (dark blue) vs. the dissipation power P_{gen} for an upward bias sweep ($I_{gen} < 0$). It deviates from the linear dependence (magenta dashed line) at $P_{gen} \simeq 0.6$ mW. (c) The temperature drop vs. I_{gen} . It is seen that ΔT is correlated with the detector response in (a). (d) The generator mesa voltage (blue, left axis) and the detector response (red, right axis) vs. P_{gen} for an upward bias sweep at another device. Black lines correspond to the reverse sweep. (e) T_{stage} vs. the dissipation power for experiments with (dark blue) and without (magenta) device for upward bias sweeps. The inset shows time dependencies of the dissipation power, identical for both cases. (f) Temperature drop (blue, left axis) and radiation power efficiency (red, right axis) vs. P_{gen} . It is seen that RPE reaches 12%.

programmable current source. The corresponding variation of T_{stage} is shown by the magenta line in Fig. 3 (e). It is almost linear with the slope $R_{th} \simeq 0.514$ K/mW. Fig. 3 (f) shows the difference between T_{stage} with and without device (blue) and the radiation power efficiency $RPE = -\Delta T / (R_{th} P_{gen})$ (red curve). It is seen that the maximum RPE for this device reaches 12%, which corresponds to the emission power of $P_{THz} \simeq 0.11$ mW. We want to emphasize that this power is actually emitted in the far-field. Indeed, it is taken out of the range cooled by the second stage of the cryocooler (which has a small cooling power) and is dumped into the first stage (with a very large cooling power), which is 10-40 cm away. This distance is much larger than the wavelength, $\lambda \sim 70$ μ m, at $f \sim 4.3$ THz. Therefore, the radiative cooling probes the total far-field emission. Of course, for the practical device the emission should be collected and delivered via open space to the desired place, which inevitably involve certain losses. In this respect the estimation of RPE from the radiative cooling provides the upper limit of the achievable “useful” emission.

Estimations above indicate that whisker-based THz sources can have $RPE > 10\%$, not far from the theoretical limit of 50% [34]. This significantly exceeds the RPE for devices made on regular Bi-2212 crystals [17, 21]. Generally, the low RPE is caused by poor impedance matching with open space [34]. JJ’s are much smaller than the

wave length. Especially tiny are interlayer distances ~ 1 nm. Therefore, JJ’s act as miniature dipoles with almost no emission in the far field. Essentially, the emission is facilitated by other passive but large-size elements of the device such as the Bi-2212 crystal and the electrodes, acting as matching antennas. Optimization of emission requires proper microwave design for impedance matching. In the Supplementary [35] we discuss the geometrical differences between crystal- and whisker-based devices. We argue that the reported boost of RPE in whisker-based devices is caused by a specific turnstile antenna-like geometry, which allows obviation of a large parasitic capacitance between the crystal and the electrode and facilitates good impedance matching with open space.

To conclude, a low radiation power efficiency is one of the main problems of THz sources. For cryogenic sources the emission power is limited both by the cooling power and RPE: $P_{THz} < RPE \times P_{cooling}$. For portable cryocoolers with limited $P_{cooling}$, the only way to increase the emission power is by enhancement of the RPE. We presented prototypes of novel THz sources based on $\text{Bi}_2\text{Sr}_2\text{CaCu}_2\text{O}_{8+\delta}$ whiskers with RPE up to 12%, more than an order of magnitude larger than for similar devices made on regular Bi-2212 crystals. This indicates better impedance matching with open space due to the specific turnstile antenna-like geometry of whisker-based devices. We argue that such devices can be used for creation of

tunable, monochromatic, continuous-wave, compact and, most importantly, power-efficient THz sources.

ACKNOWLEDGMENTS

The work was supported by the Russian Science Foundation Grant No. 19-19-00594. We are grateful to A.

Agostino and M. Truccato for assistance with whisker preparation, to S. Cherednichenko for providing the bolometer and to A. Efimov and K. Shianov for assistance in experiment. The manuscript was written during a sabbatical semester of V.M.K. at MIPT.

-
- [1] M. Tonouchi, Cutting-edge terahertz technology. *Nature Photonics* **1**, 97 (2007).
 - [2] There are also pulsed broad-band THz sources, that are fairly well developed today, for a review see e.g. P. Salen, et al., Matter manipulation with extreme terahertz light: progress in the enabling THz technology. *Phys. Rep.* **836-837**, 1-74 (2019). Such sources are beyond the scope of our paper, which is focusing on monochromatic CW sources.
 - [3] The dissipation power is $P = IV$, where I and V are bias current and voltage at the operation point of the device. Other definitions are also used, such as the wall plug efficiency, which also takes into account, e.g., the power required for refrigeration of the device. However, we use our RPE definition because operation of the cryogenic device is limited primarily by self-heating and, therefore, its performance depends solely on the power dissipated inside the cryostat.
 - [4] M. Razeghi, Q. Y. Lu, N. Bandyopadhyay, W. Zhou, D. Heydari, Y. Bai, and S. Slivken, Quantum cascade lasers: from tool to product. *Optics Express* **23**, 229245 (2015).
 - [5] M. A. Belkin and F. Capasso, New frontiers in Quantum Cascade Lasers: high performance room temperature terahertz sources. *Phys. Scripta* **90**, 118002 (2015).
 - [6] A. Khalatpour, A. K. Paulsen, C. Deimert, Z.R. Wasilewski, and Q. Hu, High-power portable terahertz laser systems. *Nat. Photonics* **15**, 16 (2021).
 - [7] A. Lyakh, M. Suttinger, R. Go, P. Figueiredo, and A. Todi, 5.6 μm quantum cascade lasers based on a two-material active region composition with a room temperature wall-plug efficiency exceeding 28 %. *Appl. Phys. Lett.* **109**, 121109 (2016).
 - [8] X. Wang, C. Shen, T. Jiang, Z. Zhan, Q. Deng, W. Li, W. Wu, N. Yang, W. Chu, and S. Duan, High-power terahertz quantum cascade lasers with ~ 0.23 W in continuous wave mode. *AIP Advances* **6**, 075210 (2016).
 - [9] C. A. Curwen, J. L. Reno and B. S. Williams, Broad-band continuous single-mode tuning of a short-cavity quantum-cascade VECSEL. *Nature Photonics* **13**, 855 (2019).
 - [10] C. Walther, M. Fischer, G. Scalari, R. Terazzi, N. Hoyler, and J. Faist, J. Quantum cascade lasers operating from 1.2 to 1.6 THz. *Appl. Phys. Lett.* **91**, 131122 (2007).
 - [11] K. Vijayraghavan, Y. Jiang, M. Jang, A. Jiang, K. Choutagunta, A. Vizbaras, F. Demmerle, G. Boehm, M. C. Amann, and M. A. Belkin. Broadly tunable terahertz generation in mid-infrared quantum cascade lasers. *Nature Commun.* **4**, 2021 (2013).
 - [12] M. Rösch, G. Scalari, M. Beck, and J. Faist, Octave-spanning semiconductor laser. *Nature Photonics* **9**, 42-47 (2015).
 - [13] S. Han, B. Bi, W. Zhang, and J. E. Lukens, Demonstration of Josephson effect submillimeter wave sources with increased power, *Appl. Phys. Lett.* **64**, 1424 (1994).
 - [14] P. Barbara, A.B. Cawthorne, S.V. Shitov, & C.J. Lobb, Stimulated emission and amplification in Josephson junction arrays. *Phys. Rev. Lett.* **82**, 1963 (1999).
 - [15] V.P. Koshelets & S.V. Shitov, Integrated superconducting receivers. *Supercond. Sci. Techn.* **13**, R53 (2000).
 - [16] L. Ozyuzer, A. E. Koshelev, C. Kurter, N. Gopalsami, Q. Li, M. Tachiki, K. Kadowaki, T. Yamamoto, H. Minami, H. Yamaguchi, T. Tachiki, K. E. Gray, W.-K. Kwok, and U. Welp, Emission of Coherent THz Radiation from Superconductors. *Science* **318**, 1291 (2007).
 - [17] T. M. Benseman, K. E. Gray, A. E. Koshelev, W.-K. Kwok, U. Welp, H. Minami, K. Kadowaki, and T. Yamamoto, Powerful terahertz emission from $\text{Bi}_2\text{Sr}_2\text{CaCu}_2\text{O}_{8+\delta}$ mesa arrays. *Appl. Phys. Lett.* **103**, 022602 (2013).
 - [18] U. Welp, K. Kadowaki, and Kleiner, Superconducting emitters of THz radiation. *Nature Photonics* **7**, 702 (2013).
 - [19] T. Kashiwagi, T. Yamamoto, H. Minami, M. Tsujimoto, R. Yoshizaki, K. Delfanazari, T. Kitamura, C. Watanabe, K. Nakade, T. Yasui, K. Asanuma, Y. Saiwai, Y. Shibano, T. Enomoto, H. Kubo, K. Sakamoto, T. Katsuragawa, B. Marković, J. Mirković, R. A. Klemm, and K. Kadowaki, Efficient Fabrication of Intrinsic Josephson-Junction Terahertz Oscillators with Greatly Reduced Self-Heating Effects. *Phys. Rev. Appl.* **4**, 054018 (2015).
 - [20] X. Zhou, Q. Zhu, M. Ji, D. An, L. Hao, H. Sun, S. Ishida, F. Rudau, R. Wieland, J. Li, D. Koelle, H. Eisaki, Y. Yoshida, T. Hatano, R. Kleiner, H. Wang, and P. Wu, Three-terminal stand-alone superconducting terahertz emitter, *Appl. Phys. Lett.* **107**, 122602 (2015).
 - [21] E. A. Borodianskyi and V. M. Krasnov, Josephson emission with frequency span 1-11 THz from small $\text{Bi}_2\text{Sr}_2\text{CaCu}_2\text{O}_{8+\delta}$ mesa structures, *Nat. Commun.* **8**, 1742 (2017).
 - [22] M. A. Galin, E. A. Borodianskyi, V. V. Kurin, I. A. Shereshevskiy, N. K. Vdovicheva, V. M. Krasnov, and A. M. Klushin, Synchronization of Large Josephson-Junction Arrays by Traveling Electromagnetic Waves. *Phys. Rev. Appl.* **9**, 054032 (2018).
 - [23] H. Sun, R. Wieland, Z. Xu, Z. Qi, Y. Lv, Y. Huang, H. Zhang, X. Zhou, J. Li, Y. Wang, F. Rudau, J. S. Hampp, D. Koelle, S. Ishida, H. Eisaki, Y. Yoshida, B. Jin, V. P. Koshelets, R. Kleiner, H. Wang, and P. Wu, Compact High- T_c Superconducting Terahertz emitter operating up

- to 86 K. *Phys. Rev. Appl.* **10**, 024041 (2018).
- [24] T. Kashiwagi, T. Yuasa, Y. Tanabe, T. Imai, G. Kuwano, R. Ota, K. Nakamura, Y. Ono, Y. Kaneko, M. Tsujimoto, H. Minami, T. Yamamoto, R. A. Klemm, and K. Kadowaki, Improved excitation mode selectivity of high-superconducting terahertz emitters. *J. Appl. Phys.* **124**, 033901 (2018).
- [25] H. Zhang, R. Wieland, W. Chen, O. Kizilaslan, S. Ishida, C. Han, W. Tian, Z. Xu, Z. Qi, T. Qing, Y. Lv, X. Zhou, N. Kinev, A. B. Ermakov, E. Dorsch, M. Ziegele, D. Koelle, H. Eisaki, Y. Yoshida, V. P. Koshelets, R. Kleiner, H. Wang, and P. Wu, Resonant Cavity Modes in $\text{Bi}_2\text{Sr}_2\text{CaCu}_2\text{O}_{8+x}$ Intrinsic Josephson Junction Stacks, *Phys. Rev. Appl.* **11**, 044004 (2019).
- [26] G. Kuwano, M. Tsujimoto, Y. Kaneko, T. Imai, Y. Ono, S. Nakagawa, S. Kusunose, H. Minami, T. Kashiwagi, K. Kadowaki, Y. Simsek, U. Welp, and W.-K. Kwok, Mesa-Sidewall Effect on Coherent Terahertz Radiation via Spontaneous Synchronization of Intrinsic Josephson Junctions in $\text{Bi}_2\text{Sr}_2\text{CaCu}_2\text{O}_{8+\delta}$. *Phys. Rev. Appl.* **13**, 014035 (2020).
- [27] M. Tsujimoto, S. Fujita, G. Kuwano, K. Maeda, A. Elarabi, J. Hawecker, J. Tignon, J. Mangeney, S.S. Dhillon, and I. Kakeya, Mutually Synchronized Macroscopic Josephson Oscillations Demonstrated by Polarization Analysis of Superconducting Terahertz Emitters. *Phys. Rev. Appl.* **13**, 051001(R) (2020).
- [28] Y. Saiwai, T. Kashiwagi, K. Nakade, M. Tsujimoto, H. Minami, R. A. Klemm, and K. Kadowaki, Liquid helium-free high- T_c superconducting terahertz emission system and its applications, *Jpn. J. Appl. Phys.* **59**, 105004 (2020).
- [29] K. Delfanazari, R. A. Klemm, H. J. Joyce, D. A. Ritchie, and K. Kadowaki, Integrated, Portable, Tunable, and Coherent Terahertz Sources and Sensitive Detectors Based on Layered Superconductors. *Proc. IEEE* **108**, 721-734 (2020).
- [30] M. A. Galin, F. Rudau, E. A. Borodianskyi, V.V. Kurin, D. Koelle, R. Kleiner, V.M. Krasnov, and A.M. Klushin, Direct Visualization of Phase-Locking of Large Josephson Junction Arrays by Surface Electromagnetic Waves. *Phys. Rev. Appl.* **14**, 024051 (2020).
- [31] V. M. Krasnov, A. Yurgens, D. Winkler, P. Delsing, and T. Claeson, Evidence for Coexistence of the Superconducting Gap and the Pseudogap in Bi-2212 from Intrinsic Tunneling Spectroscopy. *Phys. Rev. Lett.* **84**, 5860 (2000).
- [32] V. M. Krasnov, Temperature dependence of the bulk energy gap in underdoped $\text{Bi}_2\text{Sr}_2\text{CaCu}_2\text{O}_{8+\delta}$: Evidence for the mean-field superconducting transition. *Phys. Rev. B* **79**, 214510 (2009).
- [33] R. Kleiner and P. Müller, Intrinsic Josephson effects in high- T_c superconductors. *Phys. Rev. B* **49**, 1327 (1994).
- [34] V. M. Krasnov, Coherent flux-flow emission from stacked Josephson junctions: Nonlocal radiative boundary conditions and the role of geometrical resonances. *Phys. Rev. B* **82**, 134524 (2010).
- [35] See the supplementary material at ... for additional information about: A. Sample fabrication; B. Experimental setup; C. Switching current detection in on-chip generation-detection experiment; D. Supplementary video of on-chip generation-detection; and E. Discussion of geometrical advantages of whisker devices.
- [36] V. M. Krasnov, A. Yurgens, and P. Delsing, Self-heating in small mesa structures. *J. Appl. Phys.* **89**, 5578 (2001).
- [37] V. M. Krasnov, M. Sandberg and I. Zogaj, *In situ* Measurement of Self-Heating in Intrinsic Tunneling Spectroscopy. *Phys. Rev. Lett.* **94**, 077003 (2005).
- [38] S. Cherednichenko, V. Drakinskiy, T. Berg, P. Khosropanah, and E. Kollberg, Hot-electron bolometer terahertz mixers for the Herschel Space Observatory, *Rev. Sc. Instr.* **79**, 034501 (2008).
- [39] Motzkau, H. PhD Thesis: High-frequency phenomena in small $\text{Bi}_2\text{Sr}_2\text{CaCu}_2\text{O}_{8+x}$ intrinsic Josephson junctions. Stockholm University 2015, ISBN 978-91-7649-157-7.
- [40] The spectral selectivity is determined solely by the antenna. The bolometer itself has a much broader frequency range and can operate at such a frequency, as demonstrated by P. Khosropanah, J.R. Gao, W.M. Laauwen, M. Hajenius, and T.M. Klapwijk, Low noise NbN hot electron bolometer mixer at 4.3 THz. *Appl. Phys. Lett.* **91**, 221111 (2007).